

UNVEILING THE ACTIVE NUCLEUS OF CENTAURUS A¹

ALESSANDRO MARCONI
Osservatorio Astrofisico di Arcetri
Largo E. Fermi 5,
I-50125 Firenze, ITALY
e-mail: marconi@arcetri.astro.it
ETHAN J. SCHREIER, ANTON KOEKEMOER

Space Telescope Science Institute
3700 San Martin Drive,
Baltimore, MD 21218, USA
e-mail: schreier@stsci.edu
ALESSANDRO CAPETTI
Osservatorio Astronomico di Torino
Strada Osservatorio 20,
I-10025 Pino Torinese, ITALY
e-mail: capetti@to.astro.it

DAVID AXON
Department of Physical Sciences
University of Hertfordshire
College Lane,
Hatfield, Herts AL10 9AB, UK
e-mail: dja@star.herts.ac.uk

DUCCIO MACCHETTO²
Space Telescope Science Institute
3700 San Martin Drive,
Baltimore, MD 21218, USA
e-mail: macchetto@stsci.edu

AND

NICOLA CAON
Instituto de Astrofisica de Canarias
c/ via Lactea s/n,
E-38200 La Laguna, Tenerife, SPAIN
e-mail: ncaon@ll.iac.es
Draft version July 15, 2021

ABSTRACT

We report new HST *WFPC2* and *NICMOS* observations of the center of the nearest radio galaxy Centaurus A (NGC 5128) and discuss their implications for our understanding of the active nucleus and jet. We detect the active nucleus in the near-IR (K and H) and, for the first time, in the optical (I and V), deriving the spectral energy distribution of the nucleus from the radio to X-rays. The optical and part of the near-IR emission can be explained by the extrapolation of the X-ray power law reddened by $A_V \sim 14$, a value consistent with other independent estimates.

The 20pc-scale nuclear disk discovered by Schreier et al. (1998) is detected in the [FeII] λ 1.64 μ m line and presents a morphology similar to that observed in Pa α with a [FeII]/Pa α ratio typical of low ionization Seyfert galaxies and LINERs. NICMOS 3 Pa α observations in a 50'' \times 50'' circumnuclear region suggest enhanced star formation ($\sim 0.3M_{\odot} \text{ yr}^{-1}$) at the edges of the putative bar seen with ISO, perhaps due to shocks driven into the gas.

The light profile, reconstructed from V, H and K observations, shows that Centaurus A has a core profile with a resolved break at $\sim 4''$ and suggests a black-hole mass of $\sim 10^9 M_{\odot}$. A linear blue structure aligned with the radio/X-ray jet may indicate a channel of relatively low reddening in which dust has been swept away by the jet.

Subject headings: galaxies: active — galaxies: elliptical — galaxies: individual (NGC 5128, Centaurus A) — galaxies: jets — galaxies: nuclei — galaxies: Seyfert

1. INTRODUCTION

Centaurus A (NGC5128), the closest giant elliptical galaxy hosting an active galactic nucleus (AGN) and a jet, is an ideal benchmark for testing and addressing some open

issues in the unified model of AGNs. Its relative proximity ($D \sim 3.5$ Mpc, Hui et al. 1993) offers a unique opportunity to investigate the putative supermassive black-hole, the associated accretion disk and jet, i.e. the entities which the unified model considers at the core of AGN activity (see

¹Based on observations with the NASA/ESA *Hubble Space Telescope*, obtained at the Space Telescope Science Institute, which is operated by AURA, Inc., under NASA contract NAS 5-26555

²Affiliated to ESA scientific division

FIG. 1.— Grayscale representation of the mosaic in the WFPC2 F814W filter. Surface brightness ranges from 0 (white) to 1.6 in units of 10^{-16} erg s $^{-1}$ cm $^{-2}$ Å $^{-1}$ arcsec $^{-2}$. Image sizes are $225'' \times 170''$. North is up and East is left.

FIG. 2.— Grayscale representation of the mosaic in the WFPC2 F555W filter. Surface brightness ranges from 0 (white) to 1.2 in units of 10^{-16} erg s $^{-1}$ cm $^{-2}$ Å $^{-1}$ arcsec $^{-2}$. Sizes and orientation of image are as in Fig. 1.

Wills 1999 for a recent review). The detailed structure of the galaxy and the stellar and globular cluster populations can be linked to study the relationship between star formation and nuclear activity; it should be possible to assess the role of the merger in the evolution of the giant elliptical galaxy, its multiple populations and the triggering and fueling of the AGN itself. However, the study of this nearest giant elliptical at intermediate wavelengths has been severely hindered by the presence of a dust lane which dominates ground-based optical and near-IR observations of the nuclear region. The dust lane, which obscures the inner half kiloparsec of the galaxy, with associated gas, young stars and HII regions, is interpreted as the result of a relatively recent merger event between a giant elliptical galaxy and a small, gas rich, disk galaxy (Baade & Minkowski 1954, Graham 1979, Malin, Quinn & Graham 1983). See Israel (1998) for a recent comprehensive review on Centaurus A.

The presence of the AGN was revealed and studied through its radio and X-ray manifestations. Centaurus A is a giant double-lobed radio source, first discovered by Bolton, Stanley & Slee (1949) and it is considered a prototype low luminosity Fanaroff-Riley Class I radio galaxy. Its nucleus was found to be a source of X-ray emission (Bowyer et al. 1970, Kellogg et al. 1971, Grindlay et al. 1975). A strong jet was discovered in the X-rays (Schreier et al. 1979; Feigelson et al. 1981) and subsequently studied in the radio with the VLA (Schreier, Burns & Feigelson 1981; Burns, Feigelson & Schreier 1983; Clarke, Burns & Feigelson 1986; Clarke, Burns & Norman 1992) and VLBI (cf. Jones et al. 1996); it is the nearest extragalactic jet.

In the outer regions, ignoring the dust lane, Centaurus A is a fairly normal giant elliptical galaxy. Most of the light comes from an older stellar population, and the light distribution appears to follow a de Vaucouleurs law (cf. Graham 1979). The extensive system of shells within the extended elliptical component of the galaxy (cf. Malin, Quinn & Graham 1983) provide further evidence for a merger event occurring $\lesssim 5 - 10 \times 10^8$ yr ago.

IR and CO observations of the dust lane can be modeled by a thin warped disk (Quillen et al. 1992; Quillen, Graham & Frogel 1993) which dominates ground-based near-IR observations along with the extended galaxy emission (Packham et al. 1996 and references therein). R-band imaging polarimetry from HST with WFPC (Schreier et al. 1996; Paper I) are also consistent with dichroic polarization from such a disk. At large radii the radial light-profile is well fitted with a de Vaucouleurs law, but until now the dust lane has prevented secure measurements of the profile within the central arcminute (~ 1 kpc) of the galaxy or of the nucleus itself. Recent HST NICMOS observations in the K-band (Schreier et al. 1998, hereafter Paper II) have however revealed the presence of an unresolved (i.e. FWHM $< 0.2''$) source located at the nucleus of Centaurus A, superimposed on extended galaxy emission. A $\sim 1''$ radius emission line region centered on the

nucleus observed in Pa α was interpreted as an extended accretion disk around the AGN.

In this paper, we report new HST observations of the central region of the galaxy: two contiguous WFPC2 fields covering approximately $2'$ by $4'$ around the nucleus in the F336W, F555W and F814W bands, and NICMOS Camera 1, 2, and 3 observations of the nucleus and inner jet. We discuss the implications of these new high spatial resolution data in U through K on our understanding of the active nucleus, the jet, and the galaxy continuum emission in the innermost regions of Centaurus A.

These observations are part of an extensive continuing program to study this giant elliptical galaxy – the nucleus and jet of the nearest AGN, its stellar populations, and the relationship between its merger history and its nuclear activity. The current paper concentrates on the photometric structure of the galaxy interior to the dust lane, the spectral energy distributions of the nucleus, and the search for an optical/ir counterpart to the radio jet.

In Section 2 we discuss the observations and data reduction. The observational results are described in Section 3: Section 3.1 derives the location of the active nucleus and its spectral energy distribution; Section 3.2 presents new [FeII] $\lambda 1.64\mu\text{m}$ observations of the Pa α nuclear disk discovered in Paper II; Section 3.3 presents a reddening map and reconstructs the inner galaxy light profile; Section 3.4 presents the Pa α map which identifies the presence of several star formation regions; and Section 3.5 summarizes the observations related to the jet "Knot A". Section 4.1 discusses the implications of the spectral energy distribution of the nucleus. Section 4.2 analyses the galaxy light profile and its implications for the mass of the black hole. Section 4.3 discusses the implications of these observations on the starburst-AGN connection, and on the black hole fueling mechanism. Finally, section 4.4 analyses the effect of the jet on the circumnuclear region.

2. OBSERVATIONS AND DATA REDUCTION

Centaurus A (NGC 5128) was observed with both the Wide Field and Planetary Camera 2 (WFPC2 – Biretta et al. 1996) and the Near Infrared Camera and Multi-Object Spectrograph (NICMOS – MacKenty et al. 1997) on-board HST. The WFPC2 data were taken on August 1, 1997 and January 10, 1998; the two observations differed in telescope roll angle by approximately 180° optimizing coverage of the nucleus and dust lane region in the WFPC2 field of view. The pointings included the nucleus and Knot A in the higher resolution PC chips. The observations are logged in Tab. 1. Multiple exposures were performed in each of the F336W (U), F555W (V) and F814W (I) filters, and final images were produced by combining long and short exposures in each band, allowing removal of cosmic rays and correction for saturated pixels in the longer exposures.

The data were recalibrated with the pipeline software

FIG. 3.— Grayscale representation of the mosaic in the WFPC2 F336W filter. Surface brightness ranges from 0 (white) to 0.3 in units of 10^{-16} erg s $^{-1}$ cm $^{-2}$ Å $^{-1}$ arcsec $^{-2}$. Sizes and orientation of image are as in Fig. 1.

FIG. 4.— True color RGB (Red=F814W, Green=F555W and Blue=F336W) representation of the WFPC2 mosaic. Cutoff values for the images are as in Fig. 1, 2 and 3. Sizes and orientation of image are as in Fig. 1.

TABLE 1
OBSERVATIONS LOG.

Dataset	Filter	T_{exp} (sec)
WFPC2 Aug. 1 1997		
U4100101M	F336W	1800
U4100102M	F336W	600
U4100103M	F336W	1800
U4100104M	F336W	600
U4100105M	F555W	300
U4100106M	F555W	1000
U4100107M	F555W	1000
U4100108M	F814W	300
U4100109M	F814W	1000
U410010AM	F814W	1000
WFPC2 Jan. 10 1998		
U4100201M	F336W	1900
U4100202M	F336W	600
U4100203M	F336W	1900
U4100204M	F336W	600
U4100205M	F555W	260
U4100206M	F555W	1000
U4100207M	F555W	1000
U4100208M	F814W	260
U4100209M	F814W	1000
U410020AM	F814W	1000
NICMOS/CAM2 Aug. 11 1997		
N46D02APM	F222M	1279
N46D02B6M	F187N	2303
N46D02BHM	F190N	2303
NICMOS/CAM2 Sep. 9 1997		
N46D03POQ	F160W	2559
N46D03PXQ	F160W	2559
N46D03Q6Q	F110W	2559
NICMOS/CAM1 Aug. 14 1998		
N4WE01010	F164N	2560
N4WE01040	F166N	2560
N4WE01070	F166N	2560
N4WE010A0	F164N	2560
NICMOS/CAM3 Jun. 1998 (PID ^a 7919)		
N4K46KXJQ	F187N	768
N4K46KXKQ	F160W	192
NICMOS Archive (PID ^a 7330)		
N3ZB44010	F160W	319

^aProposal ID of GO Observations which we obtained from the archive

calwfp in the STSDAS/IRAF³ reduction package using up-to-date reference frames. Warm pixels and cosmic rays were removed (STSDAS tasks *warmpix* and *crrej*) and mosaiced images with spatial sampling of $0''.1/\text{pix}$ were obtained using the *wmosaic* task, which also corrects for the optical distortions in the four WFPC2 chips. The background was estimated from areas with the lowest count rates in large, dust-extincted regions; flux calibration was performed using the conversion factors given by Whitmore (1995).

NICMOS Camera 2 (NIC2) observations of the nucleus of Centaurus A were obtained on August 11, 1997 in the F222M (K), F187N (Pa α) and F190N (Pa α continuum) filters; these data were extensively discussed in Paper II. Deep NIC2 observations of the X-ray/Radio feature ‘‘Knot A’’, centered $\sim 20''$ NW of the nucleus, were obtained on September 9, 1997 in the F160W (H) and F110W (J) filters. NICMOS Camera 1 observations of the nucleus of Centaurus A were obtained on August, 14 1998 in the narrow band filters F164N and F166N ([FeII] and adjacent continuum). NICMOS Camera 3 (NIC3) observations with the F160W and F187N filters were carried out during the NIC3 campaign in June 1998 as part of a snapshot survey of nearby galaxies (Proposal ID 7919). Further NIC2 observations of the nuclear region of Centaurus A with the F160W filter, obtained as part of a GO snapshot survey (Proposal ID 7330), were retrieved from the HST Data Archive. All the NICMOS data were recalibrated using the pipeline software CALNICA v3.1 (Bushouse et al. 1997) and the best reference files in the Hubble Data Archive as of May 1998. For further discussion of NICMOS data reduction see Paper II. The NICMOS observations are logged in Tab. 1.

To construct full field images, to compare features seen in different observations taken at different times and with different instruments and, especially, to create color maps, we calculated the relative positions of the different pointings via cross correlation techniques. The WFPC2 observations taken at different dates were initially aligned to one another using image WCSs (World Coordinate System, see Voit et al. 1997 for a description) which provide the RA and Dec of each pixel, based on the HST Guide Star Catalogue (GSC) reference system, accurate up to $\pm 1''$ in absolute position. Final alignment was determined by fitting the positions of ~ 10 stars in the overlap region; the resulting images are found to be aligned to better than 0.3 WF pixels (i.e. $0''.03$). The NICMOS and WFPC2 images were aligned again by first using the image WCSs, and then cross-correlating selected regions with well-defined morphologies. The positions of stars observed in both WFPC2 and NICMOS images showed that the alignment was accurate to better than 0.4 NIC2 pixels ($\simeq 0''.03$).

3. RESULTS

Figures 1–3 are gray-scale representations of the WFPC2 mosaics in the filters F814W, F555W and F336W, corresponding to the standard I, V and U bands. Figure 4 is a true color (Red=F814W, Green=F555W,

Blue=F336W) representation of the above data. The scale is $0''.1/\text{pix}$.⁴

The images reveal significant detail of the filamentary structure of the dust lane as well as the presence of numerous sources over the entire field of view. These comprise both unresolved point sources and many spatially resolved globular clusters and stellar associations. Particularly prominent in the true-color image is a cluster of blue stars at the NW upper edge of the dust lane and at its southern edge, clearly manifesting active star formation (Dufour et al. 1979, Paper I). The prominent dark bands at the edges of the dust lane presumably correspond to folds in the dusty molecular disk proposed as responsible for the observed obscuration by Quillen, Graham & Frogel (1993). Photometry of the stars and stellar associations in the data will be discussed in subsequent papers.

3.1. The location of the nucleus

In Paper II, we identified a strong point source observed at $2.2\mu\text{m}$ as the active galactic nucleus of Centaurus A, via its spatial coincidence with the radio nucleus (within the $\pm 1''$ absolute positional uncertainty of the HST GSC). Although the current WFPC2 images in U, V and I do not show a prominent galactic nucleus, even with the superb spatial resolution of HST, the nucleus can be located in the optical data using the accurately aligned IR and optical images (Sec. 2). Figure 5 shows the $7'' \times 7''$ region centered around the IR peak. From left to right are shown: the NICMOS F222M data with the prominent nucleus; the similarly prominent unresolved component in the F160W image; the optical counterpart of the nucleus seen as a faint point source in the WFPC2 F814W data; and a marginally detected source in F555W. To our knowledge, these WFPC2 data contain the first unambiguous detection of the nucleus of Centaurus A at optical wavelengths. The nucleus is unresolved at all wavelengths, providing upper limits on the FWHM of the nuclear emission region of $< 0''.2$ (1.7pc) at $2.2\mu\text{m}$ and $< 0''.1$ (0.9pc) at 8000 \AA respectively.

The data allow us to derive the spectral energy distribution of the nucleus from the optical to the near-IR where, at the high spatial resolution of HST, the central source is easily isolated from the galaxy background. The SED is discussed further in Section 4.1 below. Note that the extreme steepness of the spectrum (the nucleus is $\sim 10^5$ times fainter in V than in K) has an important impact on the accuracy of the nuclear broad band photometry. The standard procedure used to flux-calibrate HST images involves multiplying the count rate by the PHOT-FLAM keyword (the conversion factor to flux units in $\text{erg s}^{-1} \text{ cm}^{-2} \text{ \AA}^{-1}$). However, this conversion factor assumes a flat continuum (i.e. a constant F_λ) which, clearly, does not apply to the Cen A nucleus, whose overall $0.5 - 2.2 \mu\text{m}$ spectrum can be approximated by a power law with spectral index -6.6 , i.e. $F_\nu \propto \nu^{-6.6}$. Therefore, the flux scale must be re-computed for each filter by convolving the filter transmission curve with the source spectrum. We adopted

³IRAF is made available to the astronomical community by the National Optical Astronomy Observatories, which are operated by AURA, Inc., under contract with the U.S. National Science Foundation. STSDAS contains HST-specific analysis routines developed at STScI.

⁴Color images available at <http://www.arcetri.astro.it/~marconi>

FIG. 5.— Nuclear region of Centaurus A in NICMOS (F222M, F160W) and WFPC2 (F814W, F555W) filters. North is up and East is left. The IR nucleus is located at the 0,0 position and crosses are drawn to help the eye in locating that position. A point source is detected in the F814W and marginally detected in the F555W.

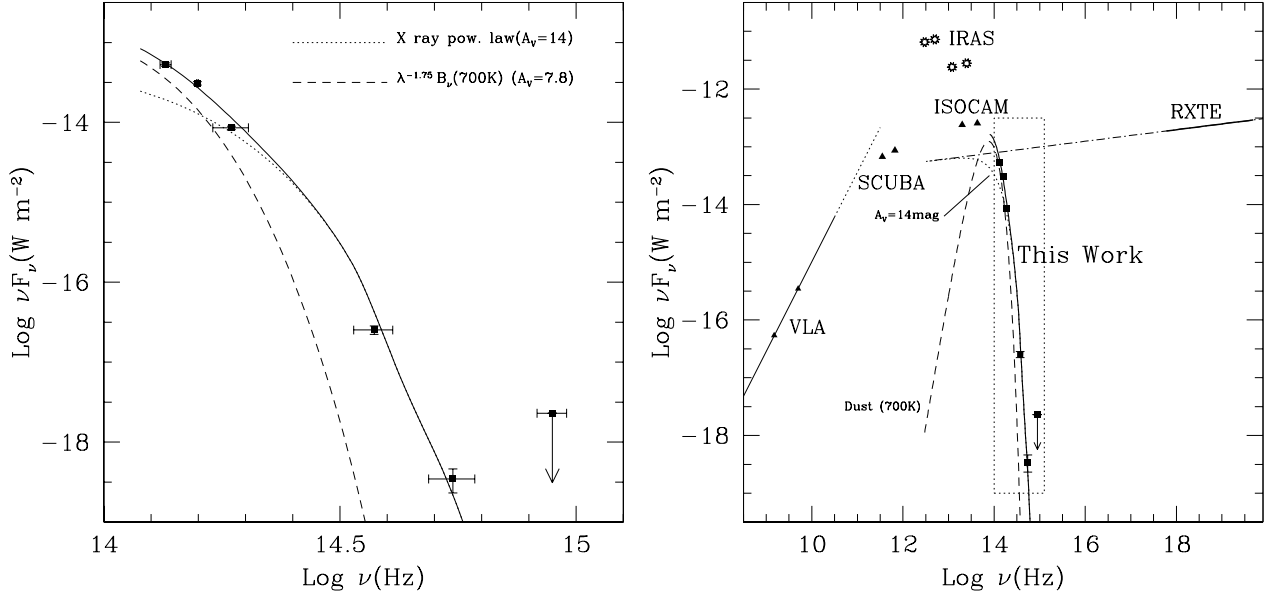


FIG. 6.— Left Panel: Nuclear photometry with WFPC2/NICMOS. Error bars along the x axis represent the width of the filters. The solid line is the spectrum resulting from the combination of (i) the power law extrapolated from the X-rays, reddened by $A_V = 14\text{mag}$ (see also right panel), and (ii) modified black-body emission at 700K (see text) reddened by $A_V = 7.8\text{mag}$. Right panel: Overall nuclear spectrum of Centaurus A. The thick line labeled “RXTE” represents the unabsorbed power law observed in the 2.5–240 keV range which is then extrapolated at lower energies (thin dash-dot-dash line). The dotted rectangle marks the limits of the graph in the left panel and the symbols in there (filled squares, thick, dashed and dotted lines) have the same meaning as above. The stars are the IRAS photometric points while the filled triangles are the SCUBA and ISOCAM photometric points from Mirabel et al. (1999). The filled circles are the radio VLA points from Burn, Feigelson & Schreier (1983) and are connected by a synchrotron spectrum. See also table 2 for values of the plotted photometric points.

an iterative procedure: using the PHOTFLAM keywords we obtained zero order flux estimates, fitted a reddened power law, and re-computed the PHOTFLAM keywords, repeating the process until it converged. The decrease of the PHOTFLAM keyword was less than 1% in F222M and F190N, but $\sim 7\%$ in F160W, and 40% and 55% for F814W and F555W respectively (see Table 2). In conclusion, it is essential to convolve the steep nucleus input spectrum with the instrumental responses. The resulting spectrum derived from our corrected HST photometry is presented in Fig. 6 (left panel) and is discussed in Sec. 4.1.

3.2. The nuclear disk

In Paper II, we presented NICMOS 2 observations in Pa α of the nuclear region of Centaurus A, which we interpreted as an inclined, ~ 40 pc diameter ionized disk. In Figure 7 we overlay on the Pa α image the intensity contours of continuum subtracted [FeII] $\lambda 1.64\mu\text{m}$ image. Morphologically, the emission in [FeII] and Pa α are almost indistinguishable and the [FeII]/Pa α ratio is $\sim 1/3$. The total detected [FeII] emission of the disk (i.e. in a $0''.9 \times 2''$ aperture) is $2.3 \times 10^{-14} \text{ erg s}^{-1} \text{ cm}^{-2}$ which is in excellent agreement with the flux of $(2.5 \pm 0.4) \times 10^{-14} \text{ erg s}^{-1} \text{ cm}^{-2}$ in a $1''.4 \times 1''.6$ aperture centered on the nucleus found by Simpson & Meadows (1998) with ground-based near-IR spectroscopy.

The ratio [FeII]/Pa $\alpha = 1/3$ corresponds to [FeII]/Br $\gamma \sim 4$ (6.6 with $A_V = 7$ and 12 with $A_V = 15$). After taking into account extinction the high [FeII]/Br γ value is typical of low excitation Seyfert galaxies and LINERs (cf. Moorwood & Oliva 1988, Alonso-Herrero et al. 1997). The much larger disks detected by HST at the centers of elliptical galaxies usually have LINER spectra, a typical example being the gaseous disk in M87 (e.g. Dopita et al. 1997).

3.3. The extended continuum emission, the reddening correction, and the galaxy light profile

The X-ray spectral low energy cutoff has long provided strong evidence for absorption along the line of sight to the Cen A nucleus. It has also long been clear from inspection of the optical images (cf. Fig. 5) that the dust lane, interpreted as a warped disk of gas and dust crossing the nuclear region, produces significant foreground obscuration. To study the SED of the nucleus, it is crucial to disentangle the foreground (disk) component from the intrinsic local absorption near the AGN. The extinction due to the dust lane also prevents a direct determination of the radial light profile near the nucleus of the galaxy in the wavelength bands observed.

We can derive an average light profile only by combining the available information in the F555W, F160W and F222M bands after estimating the respective reddening corrections. This is of course possible only assuming that no significant colour gradients are present.

We briefly present a simple, zero-order estimate to correct for reddening which, hypothesizing foreground screen extinction, is derived from the color in two bands at λ_1

and λ_2 as:

$$M_{\lambda_1}^{\circ} = M_{\lambda_1} - A(\lambda_1) = M_{\lambda_1} - \frac{R(\lambda_1)}{R(\lambda_1) - R(\lambda_2)} E(\lambda_1 - \lambda_2) \quad (1)$$

where $M_{\lambda_1}^{\circ}$ and M_{λ_1} are the intrinsic and reddened magnitudes at the effective wavelength λ_1 , $R(\lambda)$ is the extinction curve, i.e. $A(\lambda) = R(\lambda)E(B - V)$, and $E(\lambda_1 - \lambda_2) = A(\lambda_1) - A(\lambda_2)$. $E(\lambda_1 - \lambda_2)$ can be derived from the color $M_{\lambda_1} - M_{\lambda_2}$ as:

$$E(\lambda_1 - \lambda_2) = (M_{\lambda_1} - M_{\lambda_2}) - (M_{\lambda_1}^{\circ} - M_{\lambda_2}^{\circ}) \quad (2)$$

where we assume an intrinsic color, $M_{\lambda_1}^{\circ} - M_{\lambda_2}^{\circ}$, constant over the entire field of view. Different point spread functions (PSFs) are taken into account by convolving each image with the PSF of the other. We have adopted the reddening curve by Cardelli, Clayton and Mathis (1989) according to which $R(\text{F555W}) = 3.20$, $R(\text{F814W}) = 1.88$, $R(\text{F160W}) = 0.58$ and $R(\text{F222M}) = 0.35$.

Using the above formalism, we construct an E(B-V) map for the nuclear region by combining the F160W (H) and F222M (K) NICMOS images. These are more suitable for the reddening determination than the V and I band fluxes, which drop to undetectable levels in many of the heavily reddened regions of the dust lane. We assume an intrinsic colour $H - K = 0.2$ which is an average value for both spiral bulges and elliptical galaxies with a standard deviation of only 0.1 magnitudes (e.g. Hunt et al. 1997 and references therein). Note that the color correction due to the non-standard NICMOS filters is negligible (0.2 in Johnson's system corresponds to 0.24 in NICMOS).

To qualitatively verify the accuracy of the correction procedure, we apply the reddening correction to the F814W WFPC2 image. Figure 8 shows the F222M image, the E(B-V) image derived from H-K, the uncorrected and reddening corrected F814W images. The corrected F814W image is seen to be mostly smooth, similar to the F222M image which is obviously little affected by reddening. The correction fails only in a region of high extinction below the nucleus (i.e. the fold of the molecular disk, see Quillen, Graham & Frogel 1993) where E(B-V) reaches values higher than ~ 4 mag. A small linear structure starts below the nucleus and extends NW across the dust lane. The extinction in the regions immediately surrounding the nucleus is $E(B - V) \sim 2.5$ mag, in good agreement with the estimate of $A_V \sim 7$ mag given by Schreier et al. (1996). This value can be considered as a lower limit to the extinction of the nuclear light, caused by foreground extinction. In the rest of the field, apart from patches like a knot north of the nucleus ($E(B - V) \sim 2$), the extinction generally decreases from south to north, perpendicularly to the dust lane, reaching values as low as 0.1.

The reddening corrections allow us to combine data taken in different bands and reconstruct the galaxy radial light-profile. We combine the NIC2 (F222M) data, with its rather small ($r < 10''$) field of view, with the larger FOV NIC3 (F160W) data (reddening correction derived from the I-H color) and the WFPC2 (F555W) data (reddening correction derived from the V-I color). Distortions caused by the patchy reddening extinction are well corrected in the azimuthal average, as can be seen in Fig. 9 (left panel), where the H and K band light profiles after

FIG. 7.— Surface Brightness contours of the NIC1, continuum subtracted [FeII] image overlaid on a grayscale representation of the NIC2 Pa α image (Paper II). The contours are logarithmically spaced by 0.2dex and the lowest contour level is 1.5×10^{-15} erg cm $^{-2}$ s $^{-1}$ arcsec $^{-2}$. The gray scales are between -2 and 25 in units of 10^{-15} erg cm $^{-2}$ s $^{-1}$ arcsec $^{-2}$. North is up and East is left.

FIG. 8.— F222M (K) image of the nuclear region and E(B-V) map derived from the H-K colors. Observed and dereddened F814W images (nuclear region only). North is up and East is left. Each square has the size of the NICMOS 2 field of view ($20'' \times 20''$).

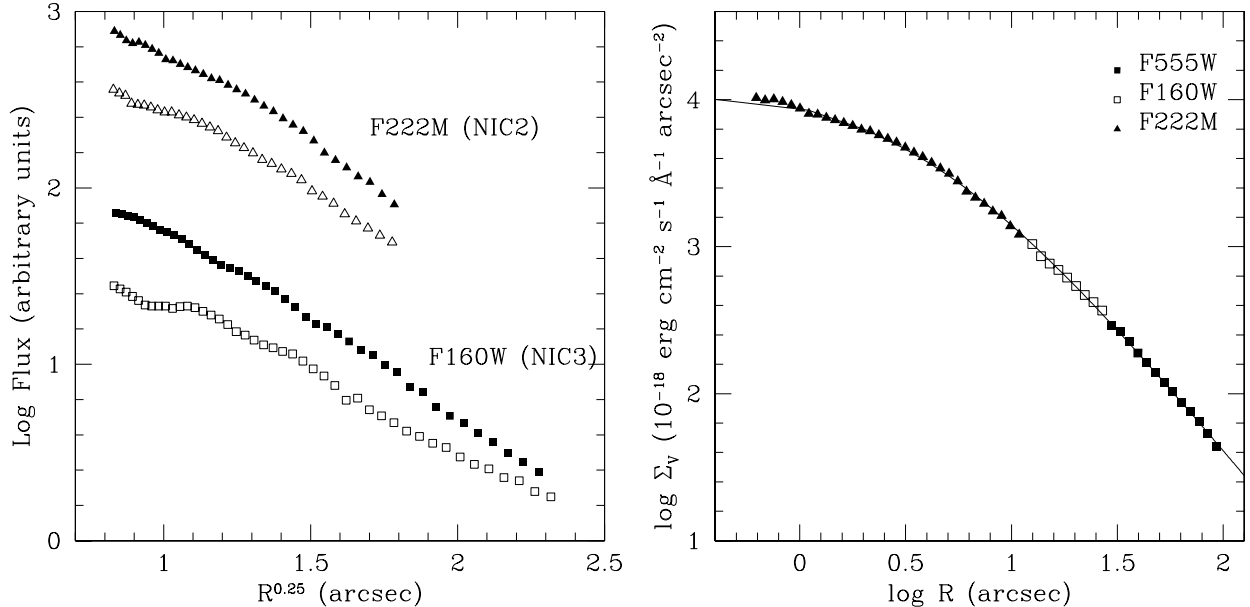


FIG. 9.— Left Panel: Effect of reddening correction on the nuclear light profiles for the F160w and F222M filter. Empty symbols are the light profiles before reddening correction. Right panel: Reconstructed nuclear profile in the V band. Measurements from H and K band were rescaled to match the V band observations. The solid line is the best fitting “Nuker-Law” (see text).

reddening correction (filled symbols) are smoother than those before correction (empty symbols); as expected, the improvement is more evident in the H band.

The overall radial profile of the nuclear region of is shown in Fig. 9 (right panel). The filled squares represent the points derived from the F555W data, the filled triangles from the F222M data, and the empty squares from the F160W data. The light profiles from the F160W and the F222M image are normalized to match that of the F555W image, using scaling factors determined from fitting the light profiles. We use the “nuker-law,” an empirical expression introduced by Lauer et al. (1995), to fit the core properties of elliptical galaxies observed at HST resolution:

$$I(r) = 2^{\frac{\beta-\gamma}{\alpha}} I_b \left(\frac{r_b}{r}\right)^\gamma \left[1 + \left(\frac{r}{r_b}\right)^\alpha\right]^{\frac{\gamma-\beta}{\alpha}} \quad (3)$$

where $I(r) \propto r^{-\gamma}$ at the center, $I(r) \propto r^{-\beta}$ at larger radii, and the transition occurs at r_b with surface brightness I_b . α represents the sharpness of the transition.

The fit parameters, including the scaling factors from H to V (S_H) and K to V (S_K), are determined via χ^2 minimization. Since it is not possible to correctly normalize the χ^2 in order to perform a statistical analysis (see sec. 4.1 of Carollo et al. 1997 for an extensive discussion) we estimated uncertainties by mapping the χ^2 in the parameter space. For a thousand times, we randomly selected the starting values of the fit parameters and let the minimization algorithm converge to find all local minima of

χ^2 . Acceptable fits were then selected by means of visual inspection.

The results of the fit are $I_b=2.5-5$ (10^{-15} erg cm $^{-2}$ s $^{-1}$ \AA^{-1} arcsec $^{-2}$), $R_b=3.3''-5.6''$, $\alpha=0.8-1.6$, $\beta=1.6-2.0$ and $\gamma=0.0-0.3$. The best fit solid line in the figure has $I_b=3.9$, $R_b = 3.9''$, $\alpha=1.0$, $\beta = 1.8$, $\gamma = 0.0$ and the scaling factors $\log S_H = 0.50$ and $S_K = 0.86$ (in log). The relatively large confidence bands for the model parameters arise because of the uncertainties in the scaling factors and the small range of radius available for fitting. Never-the-less, the profile appears to fit the data well. We discuss the implications of the radial profile in Section 4.2.

3.4. Pa α emission in the dust lane

The NIC3 F160W image and a continuum subtracted Pa α (F187N) image are presented in Figure 10, along with a 6 cm radio contour overlay (discussed further in the next section). Since no NIC3 narrow band continuum image is available, we derive one from the F160W image. To account for reddening, we estimate E(B-V) by comparing the F160W image with the WFPC2 F814W image (the F222M image used earlier has too small a field of view) and then apply the differential reddening correction to F160W to match that of F187N. The results, as seen in the figure, appear reasonable – most of the field is devoid of emission, and the structures due to reddening which appear in a direct line-continuum subtraction have disappeared. Moreover, the morphology of the nuclear region, with the disk and bow-shock like features, is the same as seen in

FIG. 10.— NICMOS 3 F160W (Left Panel) and continuum subtracted Pa α (right panel) images. North is up and East is left. Each square has the size of NICMOS 3 field of view ($50'' \times 50''$). VLA radio contours are overlaid on the Pa α image (see text).

the NIC2 Pa α continuum-subtracted data, as presented in Paper II.

Two chains of emission line knots are observed above and below the nucleus, roughly parallel to the dust lane. These are located in the regions of higher extinction – on the folds of the putative warped disk. Apart from the Pa α emission knots close to the nucleus, already extensively discussed in Paper II, the radio overlay shows no obvious correlation with the jet, in contrast with previous HST observations of Seyfert or radio galaxies with radio jets (e.g. Capetti et al. 1997, Axon et al. 1998 and references therein). The fluxes from the more intense Pa α knots are of order $\sim 2 \times 10^{-14}$ erg cm $^{-2}$ s $^{-1}$ in a $2'' \times 2''$ area, corresponding to $\sim 5 \times 10^{50}$ ph s $^{-1}$ H-ionizing photons (using $D=3.5$ Mpc and $A_V = 7$ mag as a reddening estimate in the regions of star formation). The total flux associated to these knots is $\sim 1.3 \times 10^{-12}$ erg cm $^{-2}$ s $^{-1}$.

3.5. The Jet and "Knot A"

There is a remarkable correspondence between the radio jet and the broad-band V-I color map, as seen in Fig. 11. A relatively blue linear feature coincides with the trajectory of the radio jet from the nucleus to the so-called "Knot A", well known since early X-ray/radio observations and stretching from $15''$ to $30''$ NW of the nucleus, as indicated in the figure. Faint emission in this "blue channel" is also apparent in the F336W image (upper right panel in Fig. 11).

The F160W and F110W NIC2 images of the region around Knot A are displayed in Fig. 12 along with the F814W and F555W WFPC2 images (rescaled and aligned via the cross-correlation technique described in Sec. 2). The figure also overlays 6cm VLA radio contours (E. Feigelson, private communication) on the F110W-F160W and F555W-F814W images. The radio is overlaid on the optical-infrared image by aligning the radio and infrared nuclei. Although there is no obvious optical emission correlated with the radio knots, there does appear to be a correlation between the radio and the near-IR/optical colors: the radio contours lie in a region of bluer continuum emission, similar to that observed in the linear region discussed above. Particularly intriguing is the presence of redder spots, apparently coincident with bends in the radio jet. These red spots might represent dense, dusty clouds which deflect the radio jet. It is worth noting that we do not detect any line or continuum emission associated with this putative interaction region.

We have investigated the possibility that continuum emission from the jet might be present but "masked" by galaxy emission and the patchy extinction. Using as a template the spectrum of a blue, bright region far from Knot A, we find that within statistical errors, knot A has the same spectral shape, but with different scaling factors and $E(B-V)$, implying no significant emission from the jet itself. Note also that an extrapolation of the radio synchrotron spectrum to the optical would not predict any detectable flux.

4. DISCUSSION

4.1. The Active Nucleus and its Spectral Energy Distribution

Fig. 6 (right panel) compares our photometry of the nucleus of Centaurus A with selected measurements from the literature (see also Table 2).

In X-rays, the 2.5–240 keV spectrum observed by RXTE is well fitted by a power law (plus a Fe K-shell line) with photon index ~ 1.9 , absorbed by a column density of 9.4×10^{22} cm $^{-2}$ (Rothschild et al. 1999). In the mid-IR submm range, we consider the recent ISO and SCUBA observations of Mirabel et al. (1999). We also plot the fluxes reported by IRAS although, with its relatively poor angular resolution, these points are dominated by the extended galaxy emission; as shown by ISO, the nucleus contributes at most 10% of the total mid-IR flux (Mirabel et al. 1999). Indeed, the ISO points themselves overestimate the contribution from nucleus, since even the smallest $7''$ aperture includes significant extended galaxy emission. At radio wavelengths we employ the VLA fluxes of the nucleus of Burns, Feigelson and Schreier (1983).

The absorption toward the nucleus of Centaurus A is inferred both from X-rays and infrared observations. In X-rays the observed absorbing column density corresponds to a visual extinction of $A_V \sim 47$ mag (assuming a standard gas-to-dust ratio $A_V = 5 \times 10^{-22} N_H$). We estimate $A_V \sim 15$ mag applying the extinction curve of Draine and Lee (1984) to the the $10\mu m$ silicate absorption feature in the ISO spectrum (Mirabel et al. 1999). The two values closely follow the relationship observed in Seyfert galaxies which, on average, have $A_V^{IR} \sim (0.1 - 0.5) A_V^X$, where A_V^{IR} is the extinction determined from IR spectra and A_V^X is determined from X-ray absorbing column densities, with the assumption of galactic dust-to-gas ratio (see Sec. 3 of Granato, Danese & Franceschini 1997). We note that in Section 3.3 above we have estimated a lower limit for the extinction toward the nucleus of $E(B - V) > 2.5$.

The presence of a non-thermal source in Cen A is well established from both the X-ray and radio observations and for this reason, a power law fit of the SED of the nucleus is a viable starting hypothesis. Indeed, Packham et al. (1996) described the IR nuclear spectrum of Cen A as a power law reddened by 16 mag. However, an extrapolation of their fit underestimates our V band flux by more than a factor of 1000 while, at the same time, over-predicting the $10 \mu m$ ISO flux by a factor of 20. This drawback is common to any reddened power law – reddening can not reproduce the sharp break at $\lambda < 3.5\mu m$ unless the absorption is as large as $E(B-V) \sim 20$, making the optical emission unobservable. An intrinsically steep spectrum is also unacceptable since the observed spectrum at long wavelengths, where reddening is negligible, is essentially flat.

On the other hand, an extrapolation to the optical of the observed X-ray power law, reddened by $A_V = 14$ mag (consistent with the extinction derived from the silicate feature and from the X-ray extinction), accounts for the V

TABLE 2
NUCLEAR SPECTRUM OF CENTAURUS A.

Instrument	Wavelength	Flux	$\Delta F/F$	Notes
This Work ^a				
NICMOS/F222M	2.218	2.38E-15	5%	0.99×PHOTFLAM
NICMOS/F190N	1.900	1.62E-15	5%	1.00×PHOTFLAM
NICMOS/F160W	1.610	5.31E-16	5%	0.93×PHOTFLAM
WFPC2/F814W	0.803	3.15E-18	12%	0.60×PHOTFLAM
WFPC2/F555W	0.547	6.34E-20	33%	0.45×PHOTFLAM
WFPC2/F336W	0.337	<6.8E-19	–	1.00×PHOTFLAM
Mirabel et al. 1998 ^b				
ISOCAM/LW2	7	0.6		
ISOCAM/LW3	15	1.2		
SCUBA/450	450	13		
SCUBA/850	850	19		
IRAS photometry compiled in Mirabel et al. 1998 ^b				
IRAS	12	11.2		
IRAS	25	20.1		
IRAS	60	145		
IRAS	100	217		
Rothschild et al. 1998 ^c				
RXTE/PCA/HEXTE	2–10	3.40E-10	2%	Phot. Index $\Gamma \simeq 1.9$
Burns, Feigelson & Schreier 1983 ^d				
VLA	20	3584	3%	
VLA	6	6984	3%	

^aWavelength in μm ; Flux in $\text{erg cm}^{-2} \text{s}^{-1} \text{\AA}^{-1}$; Notes are the conversion factor used in units of PHOTFLAM

^bWavelength in μm ; Flux in Jansky

^cRange of Wavelength in keV; Flux in $\text{erg cm}^{-2} \text{s}^{-1}$

^dWavelength in cm; Flux in milli-Jansky

and I measurements without exceeding the IR points (dotted line in Fig. 6) which, therefore, must be accounted for by another component.

The infrared emission of AGNs at wavelengths longer than $2\mu\text{m}$ is usually interpreted as thermal emission from hot dust close to the active nucleus (e.g., Rieke & Lebofsky 1981). The observed SED of the Cen A nucleus in the mid-infrared is also qualitatively consistent with the presence of warm dust, while the sharp drop of the nuclear intensity longward of $3\mu\text{m}$ is reminiscent of dips seen in quasar spectra, usually ascribed to the cutoff in the dust temperature distribution due to the sublimation of grains (Sanders et al. 1989). We note that silicates sublime at $T \sim 1400$ K and graphite at $T \sim 1750$ K. We test quantitatively if dust emission is consistent with the observed SED by estimating the dust temperature, T_{dust} , which corresponds to the colors measured in adjacent bands:

$$\frac{F_{\nu_1}}{F_{\nu_2}} = \frac{\lambda_1^{-\beta} B_{\nu_1}(T_{dust})}{\lambda_2^{-\beta} B_{\nu_2}(T_{dust})} \quad (4)$$

where F_ν is the dereddened flux, $B_\nu(T_{dust})$ is the blackbody function and the dust emissivity is $\epsilon_\nu \propto \nu^{-\beta}$. β is usually in the range 1.5-2 and here we assume $\beta = 1.75$. The derived temperature increases from $T \sim 250$ obtained from $F(7\mu\text{m})/F(15\mu\text{m})$, to $T \sim 920$ K for I-H, and to $T \sim 1300$ for V-I. This result is consistent with the idea that we are seeing dust with a broad temperature distribution, and that at shorter wavelengths we are sampling regions of higher temperature. However, as we have shown above, the nucleus of Cen A suffers a foreground extinction of at least $E(B-V) \sim 2.5$ and the reddening corrected V-I slope becomes incompatible with thermal emission since the corresponding temperature $T \sim 2800$ exceeds the dust sublimation temperature.

The spectrum drawn with a thick solid line in Fig. 6 (left and right panel) is the combination of two components: the extrapolation of the X-ray power law reddened by $A_V = 14$ mag and dust emission at 700K reddened by $A_V = 7.8$ mag, i.e. $E(B-V) = 2.5$ the minimum foreground extinction to the nucleus. Dust emission is described by $\lambda^{-1.75} B_\nu(700\text{K})$. This composite spectrum well reproduces the observed points: the emission in V and I is completely "non-thermal", that in K is mostly ($\sim 70\%$) thermal, while in the H band the two emission processes are comparable. Of course these results are only indicative and the emission in the near infrared could be completely dust dominated. Note that even if the 700K component fits the observed HST data points, lower temperature components are required in order to fit the ISO and SCUBA measurements. However, a complete analysis of the infrared emission spectrum is beyond the aims of this paper.

Therefore our data points on the nucleus are consistent with a scenario in which dust dominates emission in the near infrared but non-thermal emission accounts for the V and I bands and contributes to the near-IR emission. This is in agreement with previous suggestions that Centaurus A hosts a misaligned BL LAC nucleus (e.g. Bailey et al. 1986, Morganti et al. 1991, Steinle et al. 1998 and references therein). Near-IR polarimetric observations at HST resolution can further test this scenario.

Turner et al. (1992) reported that the nucleus of Cen-

taurus A at $3.5\mu\text{m}$ decreased its flux by a factor 2.5 in less than 5 years from 1987 to 1992 (comparing their data with those of Lépine et al. 1984). Comparing the surface brightness profiles and performing aperture photometry in our F160W and F187N images, obtained over 9 and 10 month baselines, respectively, we find no evidence for variability of the nucleus above the 10% level.

We note that even at the highest spatial resolution – $0''.1$, corresponding to 1.7pc or ~ 5 years – the variability reported by Turner et al. (1992) is not necessarily indicative of non-thermal emission, since the timescales are also consistent with variability in dust emission. Using the formula by Barvainis (1987) the dust sublimation radius is $\simeq 0.05\text{pc}$ (with $L_{AGN} = 10^{10}L_\odot$) therefore only variability on time scales shorter than ~ 2 months can unambiguously prove the presence of a non thermal component in the near-IR.

For completeness, even if the proposed scenario accounts for many of the properties of the Centaurus A nucleus, we note that emission in the V band could also be accounted for by a central star cluster.

4.2. The galaxy light profile and the mass of the central Black Hole

According to the classification by Faber et al. (1997), the brightness distribution of Centaurus A derived earlier is consistent with a "core" profile, with $\gamma \leq 0.3$, and with a break at a radius of ~ 3.9 . In general, galaxies with core profiles have $M_V < -22$, while those with power law profiles have $M_V > -20.5$, and both types can exist at intermediate values. Fitting a de Vaucouleurs law to the V-band isophotes of the galaxy outside the dust lane, Dufour et al. (1979) found $R_e(V) = 305''$ and estimated the total V magnitude for the elliptical component of Centaurus A as 6.20 mag which, when corrected for $E(B-V)=0.1$ of foreground extinction, becomes $V \sim 5.9$ mag. From our profile fitting of the inner region, we estimate the contribution of the central cusp, and find that the total flux is increased by $\sim 15\%$ with respect to a simple de Vaucouleurs law extrapolated in to the nucleus. This corresponds to -0.15 in magnitude i.e. $V \sim 5.75$ mag. Using a Cen A distance modulus of $(m - M)_\odot = 27.7$ (Hui et al. 1993), we find $M_V = -21.95$ (i.e. $\log L = 10.8$ in solar units), consistent with Faber's core profile classification.

Van der Marel (1999) has recently shown that the Faber classification is consistent with the hypothesis that (i) all early-type galaxies have central BHs that grew adiabatically in homogeneous isothermal cores and (ii) these "progenitor" cores follow scaling relations similar to those of the fundamental plane. This model suggests a roughly linear correlation between the mass of the central black hole and the V-band galaxy luminosity $\log M_{BH} \approx -1.83 + \log L_V$ in solar units (with an RMS scatter of 0.33 dex, or a factor two in the black hole mass). This relationship is in agreement with the average relationship for nearby galaxies with kinematically determined black hole masses (e.g. Magorrian et al. 1998). Applying the above hypotheses to the case of Centaurus A, we estimate the black hole mass to be $10^9 M_\odot$ with a factor ~ 2 RMS uncertainty. Given the large uncertainties, this value is well in agreement with a dynamical mass of $4.4 \times 10^8 M_\odot$ within 40pc, derived from H₂ spectroscopy (Israel 1998).

FIG. 11.— Overlay of the VLA radio observations on V–I grayscale. The field of view in both panels is $\sim 40'' \times 35''$. Note the correspondence between a “blue channel” and the radio contours. Knot A indicates a well known X-ray/radio feature stretching from $15''$ to $30''$ NW of the nucleus. The panel at the upper right corner represents the U grayscale where emission with a linear morphology aligned with the radio jet is marginally detected.

FIG. 12.— Upper Panels: from left to right, H, J and J–H NICMOS 2 images of the Knot A region centered $\sim 20''$ NW of the nucleus. The field of view is $\sim 20'' \times 20''$. VLA radio contours are overlaid on the J–H color image and show the stronger structures constituting Knot A. Lower Panels: from left to right, I, V and V–I WFPC 2 images. As above, radio contours are overlaid on the color image.

4.3. The Starburst-AGN connection and the fueling of the AGN

The $\text{Pa}\alpha$ emission we observe in the dust lane strongly suggests that active star formation is taking place in the circumnuclear region. We can estimate the star formation rate from $\text{Pa}\alpha$ in the inner $50'' \times 50''$ (i.e. NIC 3 field of view). As shown in section 3.4, the total observed $\text{Pa}\alpha$ flux is $1.3 \times 10^{-12} \text{ erg cm}^{-2} \text{ s}^{-1}$, which, assuming a mean extinction of $A_V = 7$, corresponds to an ionizing photon rate of $Q(H) \sim 3.1 \times 10^{52} \text{ ph s}^{-1}$. According to the models by Leitherer & Heckman (1995), the inferred Star Formation Rate (SFR) depends mostly on the assumed IMF (Initial Mass Function) slope and upper mass cutoff and just slightly on metallicity. With a Salpeter IMF and $30M_\odot$ upper mass cutoff, the continuous SFR is $0.3M_\odot \text{ yr}^{-1}$. This further decrease to $0.1M_\odot \text{ yr}^{-1}$ if the upper mass cutoff is $100M_\odot$, but increases to $1M_\odot \text{ yr}^{-1}$ with the same upper mass cutoff and a steeper IMF. In any case we find a moderately high SFR in a small ($R < 450\text{pc}$) region.

Star formation in the nuclear environment of AGNs is not uncommon. In particular local Seyfert 2 galaxies, i.e. obscured AGNs, appear characterized by enhanced circumnuclear star formation. Observational evidence comes from the strength of the far-IR continuum (Rodríguez-Espinoza et al. 1986), from mid-IR $10\mu\text{m}$ data (Maiolino et al. 1995), from the nuclear mass-to-light ratio (Oliva et al. 1999), from narrow band optical images (Gonzales-Delgado et al. 1997) and from the detection of UV spectral features typical of O stars in a sample of Seyfert 2 galaxies (Heckman et al. 1997, Gonzales-Delgado et al. 1998).

A likely explanation of this Starburst-AGN connection is that, in order to feed the AGN, large amounts of gas must be dumped in the inner Kpc of an active galaxy. The processes which can accomplish this (galaxy interactions, bars etc., see below) also trigger star formation in the dense, concentrated gas. A spectacular example of this process is given by Maiolino et al. (1999) who recently discovered a nuclear gaseous bar in the Circinus galaxy, a well known Seyfert 2.

The observed detailed morphology in $\text{Pa}\alpha$ suggests two parallel chains of star formation located in regions of high extinction N and S of the nucleus. We can relate this morphology both to the warping of a molecular disk comprising the dust lane, and also to the bar-like structure recently observed by ISO.

Quillen et al. (1992) suggested that the regions of high extinction above and below the nucleus are folds in the thin, warped molecular disk evidenced by CO emission. The extinction is higher at the folds because the disk is nearly edge-on. If star formation is taking place in this molecular disk, then the $\text{Pa}\alpha$ morphology is also easily explained, since a higher number of HII regions are projected

along our line of sight.

However, the $\text{Pa}\alpha$ emission is also seen to be correlated with the edges of the putative bar observed with ISO at 7 and $15 \mu\text{m}$ (Mirabel et al. 1999), as shown in Figure 13. This correspondence is not unexpected, since the $7\mu\text{m}$ emission is presumably dominated by PAH re-radiation, which could be excited by the hot young stars seen in $\text{Pa}\alpha$. Note that the more diffuse IR emission can be attributed to older (B or A) stars which still emit enough UV photons to excite the PAHs, but not enough to create the giant HII regions observed.

If the IR morphology is indeed indicative of a bar, as suggested by Mirabel et al. (1999), the observed morphology is consistent with the overall scenario which relates the onset of activity in galactic nuclei to interactions between galaxies (eg., Baade & Minkowski 1954; Toomre & Toomre 1972; Heckman et al. 1986; see also Balick & Heckman 1982, and Barnes & Hernquist 1992 for reviews). Specifically, “minor mergers” between a host galaxy and a small gas-rich companion or dwarf galaxy are regarded as an important means of fueling active nuclei (eg., Mihos & Hernquist 1994; Hernquist & Mihos 1995; Walker et al. 1996; Bahcall et al. 1997; De Robertis, Yee & Hayhoe 1998), in which case $\sim 10^8 M_\odot$ of stars, gas and dust can be dumped in toward the central regions, providing a fuel supply for the AGN. Such a scenario has long been invoked for Cen A (cf. discussion in Paper II).

Galaxy interactions are also known to be appealing mechanisms for triggering star formation via shocks induced in molecular clouds. Detailed n-body/hydrodynamic models suggest that interactions between ellipticals and small gas-rich galaxies result in the accretion of gas into the central regions of the elliptical (eg. Weil & Hernquist 1993; Mihos & Hernquist 1996), and that star formation can then be triggered via accretion shocks in molecular clouds. The gas is driven toward the center of the galaxy in response to tidal forces (Binney & Tremaine 1987; Barnes & Hernquist 1992). In Centaurus A, we see star formation regions both within the dust lane and at the edges of the putative bar.

Models predict shocks predominantly at the leading edges of such bars (cf. Athanassoula 1992, 1992). The shocks are likely to trigger star formation, explaining the observed morphology, wherein the HII region are located at the edges of the bar and along the “spiral arms”. At smaller scales, the $\text{Pa}\alpha$ “disk” around the nucleus, discussed in Paper II, could then be supplied by the gas streaming in from the bar, ionized by the AGN. Note that the orientation of the $\text{Pa}\alpha$ feature is perpendicular to the edges of the bar.

In summary, the feeding of the AGN requires gas to be driven in toward the nucleus, and the same galaxy interaction/merger which enriches the elliptical galaxy with gas,

FIG. 13.— Left Panel: Contours from the ISOCAM image at $7\mu\text{m}$. Center Panel: overlay of the ISOCAM contours on the NIC3 $\text{Pa}\alpha$ image showing the morphological association between the $\text{Pa}\alpha$ emission and the edges of the putative bar. The small right panel is the $\text{Pa}\alpha$ disk from Paper II. Note that its major axis is perpendicular to the edges of the “bar”.

can trigger star formation via shocks induced in molecular clouds.

4.4. *The Jet and the sweeping of the Interstellar Medium*

The data presented in Sec. 3.5 provide no evidence for synchrotron emission from the jet, either in the channel leading to Knot A or from Knot A itself. We note that an extrapolation of a simple synchrotron spectrum from the radio would not produce detectable optical synchrotron emission (see e.g. Paper I). In this regard, note also that we see no $\text{Pa}\alpha$ related to the jet, except possibly within a few arcseconds of the nucleus (see Paper II). We thus exclude emission from young stars whose formation might have been triggered by the interaction between the jet and the ISM. We also note that we cannot exclude free-free emission from hot shocked gas.

We suggest that the “blue channel” corresponds to a region of gas “evacuated” by the jet, causing lower extinction than the surroundings. We can investigate the feasibility of this hypothesis – the evacuation by the jet of a region of gas corresponding to the observed extent of the blue feature – given what is known about the lifetime of the source and the properties of the jet. The detailed radio studies by Schreier, Burns & Feigelson (1981), Burns, Feigelson & Schreier (1983), Clarke, Burns & Feigelson (1986) and Clarke, Burns & Norman (1992), suggest that the bulk kinetic power of the northern jet is $L_j \sim 1.8 \times 10^{43} \text{ erg s}^{-1}$, while the minimum age estimate of the inner lobes is $\tau_{\text{rad}} \sim 5 - 10 \times 10^6 \text{ yr}$. A simple, order-of-magnitude estimate of the amount of energy required to evacuate material from this region assumes it is described by a cylindrical geometry with a diameter $\sim 5''$ ($\sim 85\text{pc}$) and length $\sim 30''$ ($\sim 500 \text{ pc}$), initially filled uniformly by an ISM with density $n_{\text{ISM}} \sim 10 \text{ cm}^{-3}$. To displace this amount of material by a distance approximately equal to its length, over the lifetime of the radio source (assuming $\tau_{\text{rad}} \gtrsim 5 \times 10^6 \text{ yr}$ as a lower limit), would require it to be accelerated to a velocity $\sim 100 \text{ km s}^{-1}$ over this timescale. Assuming a constant kinetic energy input, the required kinetic energy flux into the ISM is therefore $F_E \sim 2 \times 10^{41} \text{ erg s}^{-1}$. Thus, evacuating the required volume of gas over the source lifetime would require a conversion efficiency of order $\lesssim 1\%$ of the total jet kinetic power, well within the bounds of feasibility.

The lack of strong line emission from the jet could suggest a scenario in which the surrounding ISM is relatively dense. If the interaction with the jet only results in slow shocks into the gas ($v_{\text{sh}} \lesssim 50 - 100 \text{ km s}^{-1}$), then little or no optical line emission is produced. However, the lack of $\text{Pa}\alpha$ or $\text{H}2$ suggesting no obvious star formation argues against this.

We conclude that we may indeed be seeing the channel evacuated by the jet between the AGN and the first bright X-ray/radio knot, despite the lack of detected emission from the knot itself.

5. CONCLUSIONS

Our HST *Wide Field and Planetary Camera 2* and *Near Infrared and Multi Object Spectrograph* observations of Centaurus A (NGC 5128) have provided several new insights about the active galactic nucleus.

Detection of unresolved emission in both visible light and near-IR suggests that two different emission mechanisms are required: a non-thermal component which represents an extrapolation of the X-ray power law, reddened by $A_V \sim 14$ (consistent with mid-IR and X-ray estimates), and a thermal component probably caused by emission from hot dust within 2pc of the nucleus. These results are in agreement with previous suggestions that Centaurus A harbors a misaligned BL Lac nucleus. We have shown that only variability on time scales shorter than ~ 2 months can unambiguously prove the existence of a non-thermal component in the near-IR.

We have detected the 20pc -scale nuclear disk in the $[\text{FeII}]\lambda 1.64\mu\text{m}$ line which shows a morphology similar to that observed in $\text{Pa}\alpha$ with an $[\text{FeII}]/\text{Pa}\alpha$ ratio typical of low ionization Seyfert galaxies and LINERs.

We do not see evidence for optical emission from, or star formation associated with, the radio/X-ray jet. We do detect a blue linear structure, aligned with jet and extending from the nucleus to knot A, which we interpret as a region of relatively low reddening. This feature may represent a channel in which gas and dust have been swept away by the jet, consistent with simple energetic arguments.

The data allow us to derive a map of dust extinction, $E(B-V)$, in a $20'' \times 20''$ circumnuclear region and reveal a several arcsecond long dust feature near but below the nucleus, oriented in a direction transverse to the large dust lane. This structure may be related to the bar observed with ISO and SCUBA, as reported by Mirabel et al. (1999). We find rows of $\text{Pa}\alpha$ emission knots along the top and bottom edges of the bar, which we interpret as star formation regions, possibly caused by shocks driven into the gas. The inferred star formation rates are moderately high ($\sim 0.3 M_{\odot} \text{ yr}^{-1}$). If we hypothesize, with Mirabel, that the bar represents a mechanism for transferring gas in to the center of the galaxy, then the large dust lane across the galaxy, the bar, the knots, and the inner $\text{Pa}\alpha$ disk previously reported in Paper II, all represent aspects of the feeding of the AGN. Gas and dust are supplied by a recent galaxy merger; a several arcminute-scale bar allows the dissipation of angular momentum and infall of gas toward the center of the galaxy; subsequent shocks trigger star formation; and the gas eventually accretes onto the AGN via the 20pc disk.

Reconstructing the radial light profile of the galaxy to within $0'.1$ of the nucleus by combining V, H and K measurements, corrected for reddening, shows that Centaurus A has a core profile, according to the classification of Faber et al. (1997). Using the models of van der Marel (1999), we estimate a black-hole mass of $\sim 10^9 M_{\odot}$, consistent with ground based kinematical measurements (Israel 1998). This is consistent with the presence of a strong AGN, as suggested by the large radio lobes, the jet, and the

strong X-ray emission. It further suggests that the ionized gas disk seen in Pa α (Paper II) would have relatively high rotational velocities, of order 800 km/sec. Planned high spatial resolution near-IR spectroscopy should be able to accurately determine the mass of the super-massive black hole in this nearest AGN.

A.M. acknowledge the partial support of the Italian Space Agency (ASI) through the grant ARS-98-116/22 and of the Italian Ministry for University and Research (MURST) under grant Cofin98-02-32. A.M. and A.C. acknowledge support from the STScI Visitor Program. A.K. acknowledge support through GO grants O0570/GO-7267 and O0568/GO-6578 from Space Telescope Science Institute, which is operated by the Association of Universities for Research in Astronomy, Inc., under NASA contract NAS 5-26555. We thank Nino Panagia, Tino Oliva, Marco Salvati, Roberto Maiolino and Lucia Pozzetti for helpful discussions which greatly improved this paper. We also thank Felix Mirabel and Dave Saunders for useful discussions and pre-publication access to the ISO data.

REFERENCES

- Alonso-Herrero A., Rieke M.J., Rieke G.H., Ruiz M., 1997 ApJ, 482, 747
- Athanassoula E., 1992a MNRAS, 259, 328
- Athanassoula E., 1992b MNRAS, 259, 345
- Axon D.J., Marconi A., Capetti A., Macchetto F.D., Schreier E.J., Robinson A., 1998, ApJ, 496, L75
- Baade W., Minkowski R., 1954 ApJ, 119, 215
- Bahcall J.N., Kirhakos S., Saxe D.H., Schneider D.P., 1997 ApJ, 479, 642
- Bailey J., Sparks W.B., Hough J.H., Axon D.J., 1986 Nature, 32, 150
- Balick B., Heckman T.M., 1982 ARA&A, 20, 431
- Barnes J.E., Hernquist L., 1992 ARA&A, 30, 705
- Barvainis R., 1987 ApJ, 320, 537
- Binney J., Tremaine S., 1987, "Galactic Dynamics", Princeton University Press
- Biretta J.A., et al., 1996, *WFPC2 Instrument Handbook*, Version 4.0 (Baltimore:STScI)
- Bolton J.G., Stanley G.J., Slee O.B., 1949 Nature, 164, 101
- Bowyer C.S., Lampton M., Mack J., 1971, ApJ, 161, L1
- Burns J.O., Feigelson E.D., Schreier E.J., 1983 ApJ, 273, 128
- Bushouse H., Skinner C.J., MacKenty J.W., 1997, *NICMOS Instrument Sci. Rept. 97-28* (Baltimore:STScI)
- Capetti A., Axon D.J., Macchetto F.D., 1997 ApJ, 487, 560
- Cardelli J.A., Clayton G.C., Mathis J.S., 1989 ApJ, 345, 245
- Carollo C.M., et al., 1997, ApJ, 481, 710
- Clarke D.A., Burns J.O., Feigelson E.D., 1986 ApJ, 300, L41
- Clarke D.A., Burns J.O., Norman M.L., 1992 ApJ, 395, 444
- De Robertis M.M., Yee H.K.C., Hayhoe K., 1998 ApJ, 496, 93
- Dopita M.A., et al., 1997, ApJ, 490, 202
- Draine B.T., Lee H.M., 1984 ApJ, 285, 89
- Dufour R.J., van den Bergh S., Harvel C.A., et al., 1979 AJ, 84, 284
- Faber S.M., Tremaine S., Ajhar E.A., et al., 1997 AJ, 114, 1771
- Feigelson E.D., Schreier E.J., Delvaile J.P., et al., 1981 ApJ, 251, 31
- Granato G.L., Danese L., Franceschini A., 1997 ApJ, 486, 147
- Gonzales Delgado R.M., Leitherer C., Heckman T.M., Cervino M., 1997, ApJ, 483, 705
- Gonzales Delgado R.M., Heckman T.M., Leitherer C., et al., 1998, ApJ, 505, 174
- Graham J.A., 1979 ApJ, 232, 60
- Grindlay J.E., Schnopper H., Schreier E.J., Gursky H., Parsignault D.R., 1975, ApJ, 201, L133
- Heckman T.M., Smith E.P., Baum S.A., et al., 1986 ApJ, 311, 526
- Heckman T.M., Gonzales Delgado R.M., Leitherer C., et al., 1997, ApJ, 482, 114
- Hernquist L., Mihos J.C., 1995 ApJ, 448, 41
- Hui X., Ford H.C., Ciardullo R., Jacoby G.H., 1993 ApJ, 414, 463
- Hunt L.K., Malkan M.A., Salvati M., et al., 1997 ApJS, 108, 229
- Israel F.P., 1998 A&A Rev., 8, 237
- Jones D.L., Tingay S.J., Murphy D.W., et al., 1996 ApJ, 466, L63
- Kellogg E., Gursky H., Leong C., Schreier E., Tananbaum H., Giacconi R., 1971, ApJ, 165, L49
- Lauer T.R., Ajhar E.A., Byun Y.-I., et al., 1995 AJ, 110, 2622
- Leitherer C., Heckman T.M., 1995 ApJS, 96, 9
- Lépine J.R.D., Braz M.A., Epchtein N., 1984 A&A, 131, 72
- MacKenty J.W., et al., 1997, *NICMOS Instrument Handbook*, Version 2.0 (Baltimore:STScI)
- Magorrian J., et al., 1998, AJ, 115, 2285
- Maiolino R., Ruiz M., Rieke G.H., Keller L.D., 1995 ApJ, 446, 561
- Maiolino R., Alonso-Herrero A., Anders S., et al., 1999 ApJ, submitted
- Malin D.F., Quinn P.J., Graham J.A., 1983 ApJ, 272, L5
- Mihos J.C., Hernquist L., 1994 ApJ, 425, L13
- Mihos J.C., Hernquist L., 1996 ApJ, 464, 641
- Mirabel I.F., Laurent O., Sanders D.B., et al., 1999 A&A, 341, 667
- Moorwood A.F.M., Oliva E., 1988 A&A, 203, 278
- Morganti R., Robinson A., Fosbury R.A.E., di Serego Alighieri S., Tadhunter C.N., Malin D.F., 1991 MNRAS, 249, 91
- Oliva E., Origlia L., Maiolino R., Moorwood A.F.M., 1999 A&A, submitted
- Packham C., Hough J.H., Young S., et al., 1996 MNRAS, 278, 406
- Quillen A.C., de Zeeuw P.T., Phinney E.S., Phillips T.G., 1992 ApJ, 391, 121
- Quillen A.C., Graham J.R., Frogel J.A., 1993 ApJ, 412, 550
- Rieke G.H., Lebofsky M.J., 1981 ApJ, 250, 87
- Rodriguez-Espinoza J.M., Rudy R.J., Jones B., 1986, ApJ, 309, 76
- Rothschild R.E., Band D.L., Blanco P.R., et al., 1999 ApJ, 510, 651
- Sanders D.B., Phinney E.S., Neugebauer G., et al., 1989 ApJ, 347, 29
- Schreier E.J., Feigelson E., Delvaile J., et al., 1979 ApJ, 234, L39
- Schreier E.J., Burns J.O., Feigelson E.D., 1981 ApJ, 251, 523
- Schreier E.J., Capetti A., Macchetto F., Sparks W.B., Ford H.J., 1996 ApJ, 459, 535 (Paper I)
- Schreier E.J., Marconi A., Axon D.J., Caon N., Macchetto D., Capetti A., Hough J.H., Young S., Packham C., 1998, ApJ, 499, L143 (Paper II)
- Simpson C., Meadows V., 1998 ApJ, 505, L99
- Steinle H., Bennett K., Bloemen H., et al., 1998 A&A, 330, 97
- Toomre A., Toomre J., 1972 ApJ, 178, 623
- Turner P.C., Forrest W.J., Pipher J.L., Shure M.A., 1992 ApJ, 393, 648
- van der Marel R.P., 1999 AJ, 117, 744
- Voit, M., et al., 1997, *HST Data Handbook - Vol. I*, Version 3.0 (Baltimore:STScI)
- Walker I.R., Mihos J.C., Hernquist L., 1996 ApJ, 460, 121
- Weil M.L., Hernquist L., 1993 ApJ, 405, 142
- Whitmore B., 1995, In *Calibrating HST: Post Servicing Mission*, A. Koratkar and C. Leitherer (Eds.), Baltimore STScI, p.269
- Wills B.J., in "Quasars and Cosmology", A.S.P. Conference Series (1999), eds. G.Ferland, J.Baldwin (San Francisco:ASP), in press (astro-ph/9905093)

This figure "f1.gif" is available in "gif" format from:

<http://arxiv.org/ps/astro-ph/9907378v1>

This figure "f2.gif" is available in "gif" format from:

<http://arxiv.org/ps/astro-ph/9907378v1>

This figure "f3.gif" is available in "gif" format from:

<http://arxiv.org/ps/astro-ph/9907378v1>

This figure "f4.gif" is available in "gif" format from:

<http://arxiv.org/ps/astro-ph/9907378v1>

This figure "f5.gif" is available in "gif" format from:

<http://arxiv.org/ps/astro-ph/9907378v1>

This figure "f7.gif" is available in "gif" format from:

<http://arxiv.org/ps/astro-ph/9907378v1>

This figure "f8.gif" is available in "gif" format from:

<http://arxiv.org/ps/astro-ph/9907378v1>

This figure "f10.gif" is available in "gif" format from:

<http://arxiv.org/ps/astro-ph/9907378v1>

This figure "f11.gif" is available in "gif" format from:

<http://arxiv.org/ps/astro-ph/9907378v1>

This figure "f12.gif" is available in "gif" format from:

<http://arxiv.org/ps/astro-ph/9907378v1>

This figure "f13.gif" is available in "gif" format from:

<http://arxiv.org/ps/astro-ph/9907378v1>